

Developing the tracking algorithm for Geant4 based simulated muon data, a step towards muography studies

Submitted By

Abhishek

School of Physical Sciences

National Institute of Science, Education and Research (NISER), Bhubaneswar



Under the Guidance of

Supervisor: Prof. Bedangadas Mohanty

School of Physical Sciences

National Institute of Science, Education and Research (NISER), Bhubaneswar

&

Co-supervisor: Dr. Raveendrababu Karnam

Center for Medical and Radiation Physics

National Institute of Science, Education and Research (NISER), Bhubaneswar

Acknowledgement

I would like to express my gratitude to my supervisor, Prof. Bedangadas Mohanty, for offering me the opportunity and guidance throughout this project. I am also grateful to Dr Raveendrababu Karnam, for his consistent support and assistance. Lastly, I express my thanks to Dr. Varchaswi K S Kashyap for addressing my inquiries related to the project.

Abhishek

5th Year Integrated M.Sc.

School of Physical Sciences

NISER, Bhubaneswar

Abstract

This report presents the GEANT4 simulation studies of imaging high-Z material using cosmic-ray muons. A muon telescope is developed using resistive plate chambers as the active detector elements with the GEANT4 toolkit. The Point of Closest Approach algorithm is implemented to image the high-Z materials, like Lead and Uranium. Also, this telescope can differentiate the medium and high-Z materials using scattering angle distributions.

A Resistive Plate Chamber (RPC) is developed using the glass plates of size $200 \times 200 \times 3 \text{ mm}^3$ (length \times width \times thickness). A Printed Circuit Board (PCB) based strip readout panel is developed to read the signals from the RPC.

Contents

Acknowledgement	i
Abstract	ii
	Page
1 Cosmic-ray Muography	2
1.1 Imaging with cosmic-rays muons	2
1.1.1 Absorption Muography	2
1.1.2 Scattering Muography	2
1.2 Detectors for muon tomography	3
1.2.1 Working principle of an RPC	4
2 Muoscope Simulation Setup	5
2.1 Cosmic-ray muons generator	5
2.2 Simulation Setup	6
2.3 Analysis Pipeline	7
2.4 Measurement of spatial and angular resolution of the telescope	7
2.5 Tomography	8
2.5.1 POCA Scattering points	8
2.5.2 Differentiating High-Z material using Muon Tomography	9
3 Experimental Studies	10
3.1 Building the RPC and signal read-out panel	10
3.1.1 Procedure used to build the RPC	10
3.1.2 Procedure used to develop RPC signal read-out panel	10
3.2 Future Directions	11
3.2.1 Simulations studies	11
3.2.2 Experimental Studies	11
A	12
A.1 Time dilation for Cosmic-Ray muons	12

B.2	Point of Closet Approach	13
C.3	Simulation Setup	13
D.4	Differentiating high-Z material (Iron, Lead and Uranium, Iron) using Muon Scat- tering Tomography (MST)	15
D.4.1	Scattering angle distribution for an iron block of size $100 \times 100 \times 100$ mm^3	15
D.4.2	Scattering angle distribution for uranium block size $100 \times 100 \times 100 mm^3$	16

Chapter 1

Cosmic-ray Muography

Cosmic rays are high-energy particles originating from various astrophysical sources, such as supernovae, gamma-ray bursts, and active galactic nuclei. These energetic particles mostly contain protons and small fractions of heavy nuclei, electrons, positrons and antiprotons. These particles enter into the Earth's upper atmosphere and collide with the atmospheric nuclei (mostly Nitrogen (N_2) and Oxygen (O_2)) and produce hadrons like Pions and Kaons. Pions (π^+ , π^0 , π^-) and Kaons (K^+ , K_S^0 , K_L^0 , K^-) are the hadrons most abundantly produced by these cosmic-ray collision with air molecules in upper atmosphere, and when they are charged, their dominant decay modes produce muons that are naturally abundant at sea level. More details are provided in Appendix A.1.

When muons pass through a given material, they lose their energy due to inelastic collisions with atomic electrons and deflect from their incident direction due to elastic scattering from nuclei. Muons have very high penetration capabilities since they are least likely to interact with the matter. Muography is an imaging technique that relies on the interaction of cosmic-ray muons with the object of interest.

1.1 Imaging with cosmic-rays muons

Like other charged particles, muons also interact with atoms of matter, which results in energy loss and scattering. Based on these interactions, we can divide imaging with cosmic-ray muons into absorption muography (AM) and scattering muography (SM) [1, 2].

1.1.1 Absorption Muography

This technique is based on the measurement of the attenuation of the muon flux by large, massive objects. By measuring the muon flux in the path of massive structures like mountain pyramids and comparing it to the muon flux in open, free sky muons, we can create a map estimating the density of these structures without any invasive method. This method has been applied to measure density distributions in structures like volcanoes and pyramids and to explore cavities within railway tunnels.

1.1.2 Scattering Muography

It is also known as tomography, which depends on the elastic multiple coulomb scattering of muons inside the target material. When muon passes through matter, it scatters multiple

times; therefore, the outgoing angle would differ from the incoming angle. Usually, charged particles follow Rutherford scattering distribution [3]. However, $\Delta\theta$ ($\theta_{out} - \theta_{in}$) follows the Gaussian distribution approximately since it scatters multiple times. The net angular distribution features an approximately Gaussian core, and the standard deviation can be expressed as

$$\sigma(\theta) = \frac{z \cdot 13.6 \text{ MeV}}{p\beta c} \sqrt{\frac{x}{X_0}} \left[1 + 0.038 \cdot \ln \left(\frac{x}{X_0} \right) \right] \quad (1.1)$$

Here, p and βc are the momentum and velocity of the muon, $z = 1$ is the charge of the muon and x and X_0 are the target's thickness and characteristic radiation length, respectively. The radiation length is the mean distance over which an electron loses all but $1/e$ of its energy and can be written as follows:

$$X_0 = \left[\frac{A \cdot 716.4 \text{ g cm}^{-2}}{Z(Z+1) \ln(287/\sqrt{Z})} \right] \left[\frac{1}{\rho} \right] \quad (1.2)$$

Here, ρ , A and Z are the material's density, atomic weight and atomic number. The approximate $\rho \cdot Z^2$ dependence for large Z characterises the sensitivity to dense objects with a high atomic number, a unique feature of muon scattering tomography.

This technique has been used in nuclear security and safety, transport controls, such as containers and trucks, for the detection of illicit or dangerous materials, etc.

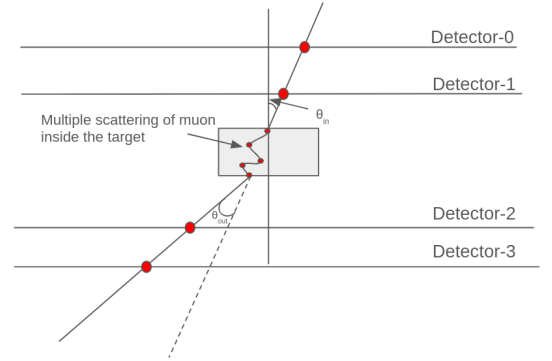


Fig. 1.1: Multiple Scattering

1.2 Detectors for muon tomography

For cosmic-ray muon imaging applications, technologies have been used are nuclear emulsion detectors, scintillation detectors and gaseous detectors, according to the kind of application.

In this project, Resistive Plate Chambers (RPC) are used as the active detector element to develop the muon telescope. RPC is a gaseous detector made of two parallel plate electrodes. It has a constant and uniform electric field in between the high-resistive electrodes. It is developed by R. Santonico and R.Cardareli [5]. RPCs have gained widespread recognition in experimental particle physics due to their application in detecting muons within various contemporary particle physics experiments, such as ATLAS [6] and CMS [7]. These chambers offer a favourable combination of precise spatial resolution and a rapid one-nanosecond time resolution. Additionally, they exhibit high efficiency and cost-effectiveness, making them a preferred choice in experimental setups. Schematic of a single gap RPC is shown in Figure 1.2.

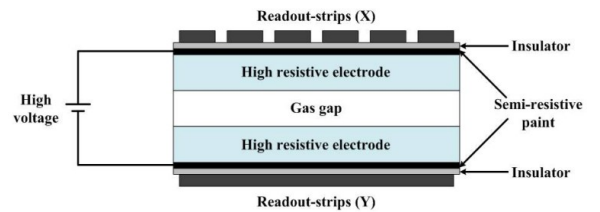


Fig. 1.2: Schematic of an RPC [4].

1.2.1 Working principle of an RPC

The RPC has a uniform electric field between two electrodes filled with a gas mixture. When a charged particle passes through the gas, it ionizes the gas medium, generating electrons and ions. The strong electric field causes the primary electrons to accelerate. Suppose the electric field is more than a threshold value. In that case, electrons will get sufficient energy to produce secondary electrons; similarly, secondary electrons will produce tertiary electrons; in this way, an avalanche multiplication will occur, producing a detectable electrical signal. Electrodes will collect this charge and produce a signal. Please see Figure 1.3. The number of ion pairs generated per unit path length is proportional to the total number of ion pairs initially generated. Let Q be the total charge produced in an avalanche:

$$Q = n_0 e M$$

where, n_0 : number of original ion pairs created M : Multiplication factor The Townsend equation describes how the number of charged pairs increases proportionally to the distance travelled along a path :

$$\frac{dN}{dx} = \alpha N \Rightarrow N(x) = N_0 e^{\alpha x}$$

where, N_0 : number of primary ion-pairs α : The First Townsend coefficient represents the rate of collisions resulting in ionization per unit length along the particle's path. x : Distance from the anode.

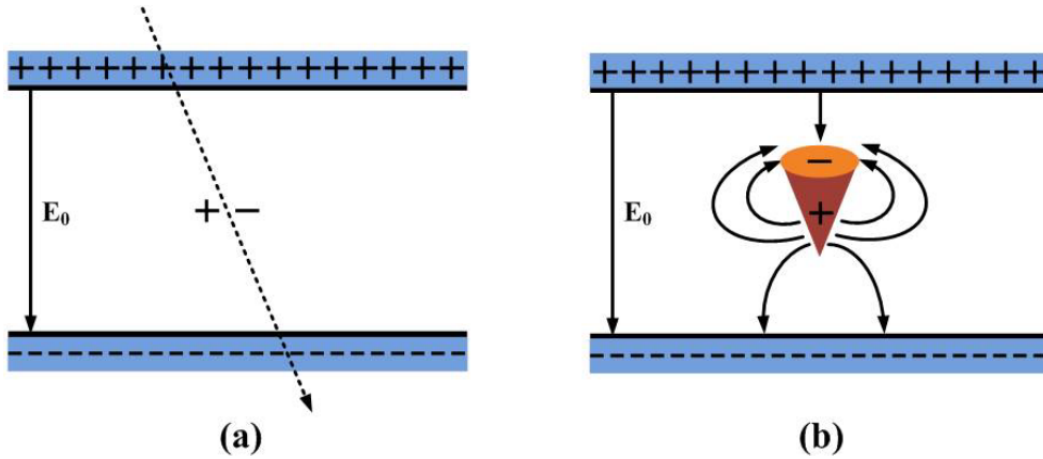


Fig. 1.3: (a) Muon ionizing gas medium and producing a pair of electrons and ions. (b) Formation of an avalanche inside the RPC and electrons are moving towards the anode, and ions are moving towards the cathode [4].

Chapter 2

Muoscope Simulation Setup

In the current project, a muon telescope is being developed for tomography applications. In the context of muon tomography, four Resistive Plate Chambers (RPC) are employed — two for the upper tracker and two for the lower tracker. The imaging target is placed between these two trackers. Before constructing an actual muoscope, we primarily aim to conduct simulations using the GEANT4 toolkit [8]. This simulation allows us to model atomic interactions between muons and the target material. After running the simulation, the data can be stored in a ROOT [9] file, enabling subsequent analyses such as computing the distribution of scattering angles and Points of Closest Approach (POCA). The project source code is on GitHub [10].

2.1 Cosmic-ray muons generator

In our study, we employed a parametric generator known as **ECoMuG:An Efficient COsmic MUon Generator for cosmic-ray muon applications**[11]. EcoMug is a header-only C++11 library that relies on a parametrization of experimental data. It allows users to generate cosmic-ray (CR) muons based on custom parametrizations of their differential flux, i.e. Gaisser distribution. In ECoMuG, the following distribution was used:

$$J'_z \equiv \frac{dN}{dt \cdot dp \cdot d\theta \cdot d\phi \cdot dS_z} = \left[1600 \cdot \left(\frac{p}{p_0} + 2.68 \right)^{-3.175} \cdot \left(\frac{p}{p_0} \right)^{0.279} \right] \cdot (\cos \theta)^{n+1} \cdot \sin \theta \cdot \frac{1}{\text{m}^2 \cdot \text{s} \cdot \text{sr} \cdot \text{GeV}/c} \quad (2.1)$$

In the flat sky generation, the origin position of generated CR muons is uniformly distributed over the generation surface. The azimuth angle ϕ is uniformly randomly generated in $[0, 2\pi]$, and the momentum and zenith angle θ are sampled from the differential flux in the above equation. Energy distribution peaks around 5.1 GeV, and zenith angle distribution follows $\cos^2 \theta$. CR muons flux is uniformly dependent on the azimuthal angle ϕ . In addition, the ratio of the number of positive muons to the number of negative muons is ≈ 1.28 [12]. All the results are shown in figure 2.1. The following are the parameters for ECoMuG.

Input Parameters

Shape (flat), position $(0, 0, -30 \text{ mm})$ and size $(160 \times 160 \text{ mm}^2)$ of generator surface.

Range of θ (Zenith angle) is $[0, \frac{\pi}{2}]$ radian and p (momentum) $> 100 \text{ MeV}$.

Particle definition of positive and negative muons.

Output Parameters

Flat sky surface generator located at the provided position.

Distribution of θ and p as per equation (2.1) and outputs are shown in Figure 2.1.

Number of positive and negative muons.

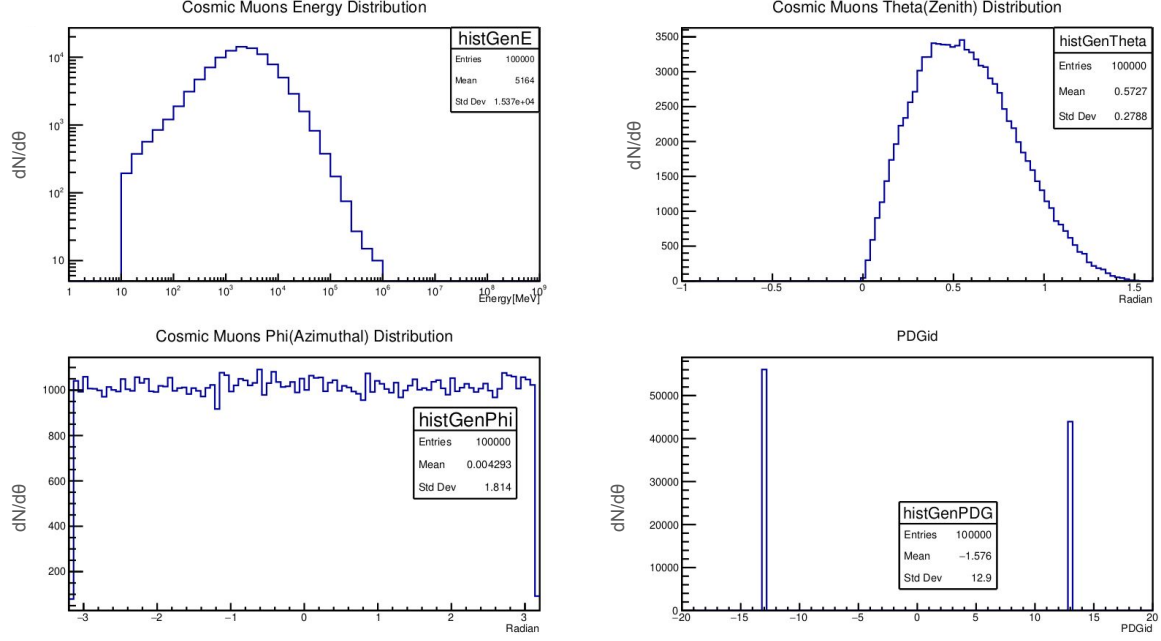


Fig. 2.1: Using EcoMug, 100000 muons are generated. The cosmic-ray muon energy, zenith angle and azimuthal angle distributions, and the flux of positive and negative muons are shown.

2.2 Simulation Setup

Muoscope geometry is built using GEANT4 toolkit [8]. Summary of Geometry: The Muoscope comprises four RPCs, featuring the upper two for tracking the incoming muons and the lower two for tracking the outgoing muons, after scattering through the target. Each RPC of active area, 160 x 160 mm², is enclosed within an acrylic box of dimensions 400 x 400 x 55 mm³, which are proposed for the realistic telescope. Each RPC comprises two graphite-coated glass plates. On each electrode, a PCB panel having 16 readout strips is mounted, and the strips on the first electrode are orthogonal to the strips on the second electrode. Each strip is 9 mm wide and 160 mm long, with a 1 mm gap between the consecutive strips. Please see the Figure 1.2. The simulated geometry of the muon telescope is shown in Figure 2.2a. The muons are generated using EcoMug from 50 mm above the top layer of RPC. The simulated muon tracks across the muon telescope are shown in Figure 2.2b.

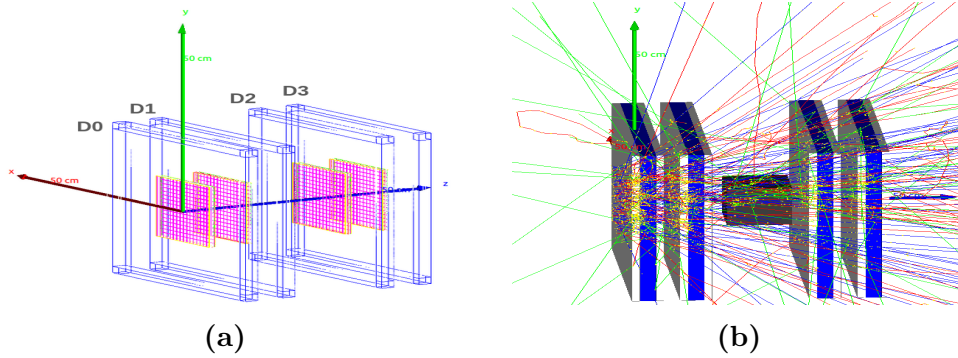


Fig. 2.2: (a) Simulated muon telescope comprising four layers of RPCs housed in acrylic boxes (D0-D3). (b) Muon tracks are generated from the top layer of RPC. The negative muon tracks are represented in red colour, the positive muon tracks in blue colour, and the green tracks depict secondary particles generated through the scattering of muons.

2.3 Analysis Pipeline

After building the geometry and shooting muons, the following steps were followed to test and store the hits: Generating CR Muons using EcoMug \rightarrow Storing each hit in the root file \rightarrow Analysing the Histograms \rightarrow Using MakeClass Method to to more rigorous analysis \longleftrightarrow imposing required constraint to obtain results \longleftrightarrow adding POCA algorithm as a header file.

2.4 Measurement of spatial and angular resolution of the telescope

In Fig.3.1 (a), First, in each detector, a hit is stored as X_{hit} . Then, a hit is removed from detector 1. A straight line is fitted using the remaining three hits, obtaining a hit value from the fitted track, denoted as X_{fit} . The residual is calculated as follows: $\text{Residual} = X_{\text{hit}} - X_{\text{fit}}$. In the XZ plane, each hit is labeled by the variables x_0 , x_2 , and x_3 . Using these variables as independent parameters and their corresponding z_0 , z_2 , and z_3 variables, we will perform linear regression to fit a track $z = mx + c$ using the following coefficients:

$$m = \frac{n(\sum xz) - (\sum x)(\sum z)}{n(\sum x^2) - (\sum x)^2} \quad \text{and} \quad c = \frac{\sum z - m(\sum x)}{n} \quad (2.2)$$

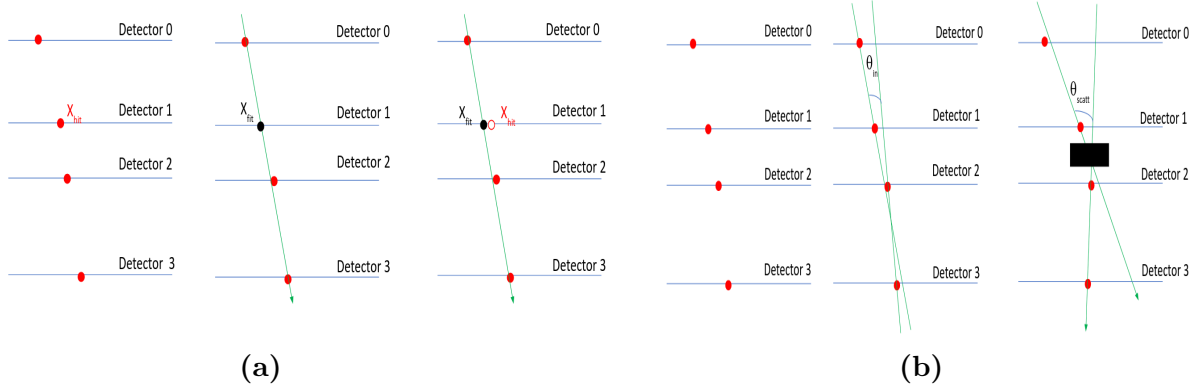


Fig. 2.3: Illustration for determining (a) the spatial resolution and (b) the angular resolution.

If these residuals are plotted, the distribution is observed to be Gaussian (figure 2.4a). The hit position resolution (σ) can be determined from the spread of the Gaussian distribution: Hit (position) resolution = $\sigma(\text{Residual})$.

Angular resolution is evaluated by recording hits in the upper trackers and extrapolating a line $\mathbf{d}_0\mathbf{d}_1$. Similarly, for lower tracker extrapolating a line $\mathbf{d}_2\mathbf{d}_3$, then using the dot product, we can compute the scattering angle between these two lines $\mathbf{d}_0\mathbf{d}_1 \cdot \mathbf{d}_2\mathbf{d}_3 = \|\mathbf{d}_0\mathbf{d}_1\| \times \|\mathbf{d}_2\mathbf{d}_3\| \cos(\theta)$

Where θ is calculated as following

$$\theta = \arccos\left(\frac{\mathbf{d}_0\mathbf{d}_1 \cdot \mathbf{d}_2\mathbf{d}_3}{\|\mathbf{d}_0\mathbf{d}_1\| \times \|\mathbf{d}_2\mathbf{d}_3\|}\right)$$

The angular resolution is determined by analyzing the distribution of scattering angles between the two tracks, following a Gaussian distribution. The detector's obtained spatial and angular

resolutions can be applied to introduce noise into simulated data, enhancing its resemblance to actual experimental data. Furthermore, the angular resolution serves as an offset for the scattering angle measurement distribution. While ideally, there should be no scattering in the absence of objects, the presence of materials like the acrylic box results in finite scattering. The angular resolution is a corrective offset in mitigating this observed scattering effect.

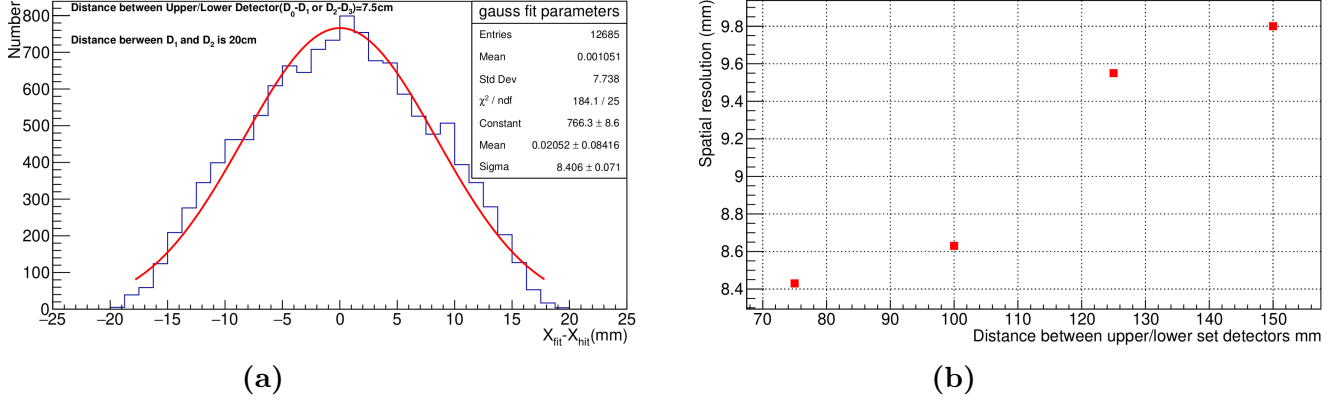


Fig. 2.4: (a) The residuals, resulting in a Gaussian distribution with a standard deviation of 8.43 mm; (b) The spatial resolution as a function of the distance between the d0-d1 and d2-d3.

2.5 Tomography

- $\vec{X} \rightarrow$ Input variables for a given dynamical system. Example: Position/direction of a muon at the upper detector. (Known)
- $\vec{f} \rightarrow$ Physics laws governing the evolution of the system. Notice: It can be deterministic but also probabilistic. Example: Moliere's scattering formula for angular deviations. (Known)
- $\vec{\theta} \rightarrow$ Parameters describing the physics environment. Example: Densities and geometry of the crossed material. (Unknown)
- $\vec{y} \rightarrow$ Output variables after the action of \vec{f} . Example: Position/direction of a muon at the lower detector. (known)

Therefore, we can compute $\vec{y} = \vec{f}(\vec{X}; \vec{\theta})$

2.5.1 POCA Scattering points

The Point of Closest Approach (POCA) algorithm is a mathematical method used to find the closest distance between two lines or tracks that move in three-dimensional space but do not necessarily intersect. A detailed derivation is available in the appendix (B.2). The implementation in C was sourced from [13], and I have adapted it for our analysis.

The objective is to find the shortest line segment connecting two tracks (2.5a). This can be accomplished by considering that the shortest line will be perpendicular to both tracks. Thus, the dot product of this line with two skew lines will be zero for each line. Using this condition allows us to find such a line; see more details in appendix (B.2). The midpoint of the $\overline{P_a P_b}$ line is the POCA point. A $100 \times 100 \times 100 \text{ mm}^3$ lead block (see fig 2.2b) is imaged using this algorithm. A 2D histogram (fig 2.5b) is generated by POCA points to visualize an image of a lead block with dimensions $100 \times 100 \times 100 \text{ mm}^3$.

2.5.2 Differentiating High-Z material using Muon Tomography

During the simulation, we positioned a lead(Pb, $Z=82$) block with dimensions of $10 \times 10 \times 10 \text{ cm}^3$. Subsequently, we measured the deviation between the incoming and outgoing tracks in the XZ and YZ planes. The resulting distribution follows a Gaussian distribution, with the standard deviation (σ) determined by (1.1). For Lead radiation decay, the length is given by (1.2), with an average momentum of approximately 5.2 GeV for atmospheric muons, the standard deviation of the scattering angle is calculated to be 12.05 milliradians. The obtained result from the simulation is 12.34 mrad (see fig 2.6b), which is closely aligned with the theoretical formula. This technique effectively distinguishes materials with higher atomic numbers (Z). See the appendix (D.4) for different types of materials.

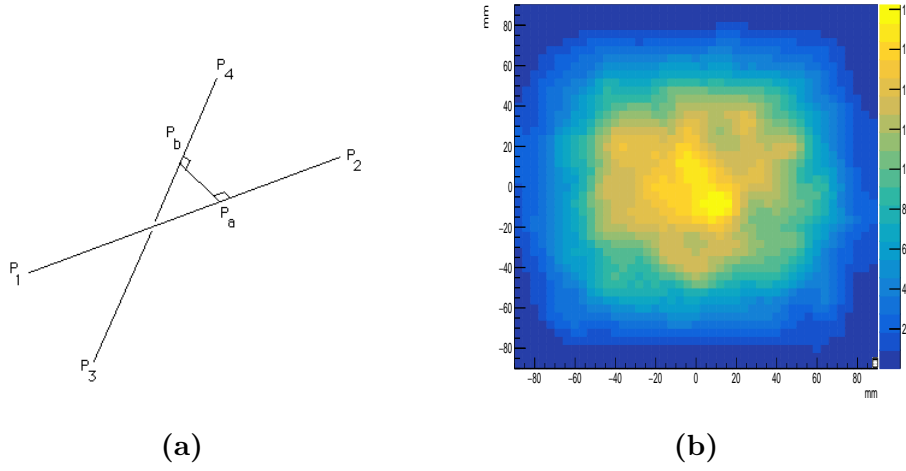


Fig. 2.5: (a) Two tracks in three dimensions; and (b) POCA reconstructed image of a $100 \times 100 \times 100 \text{ mm}^3$ lead block using the muon telescope.

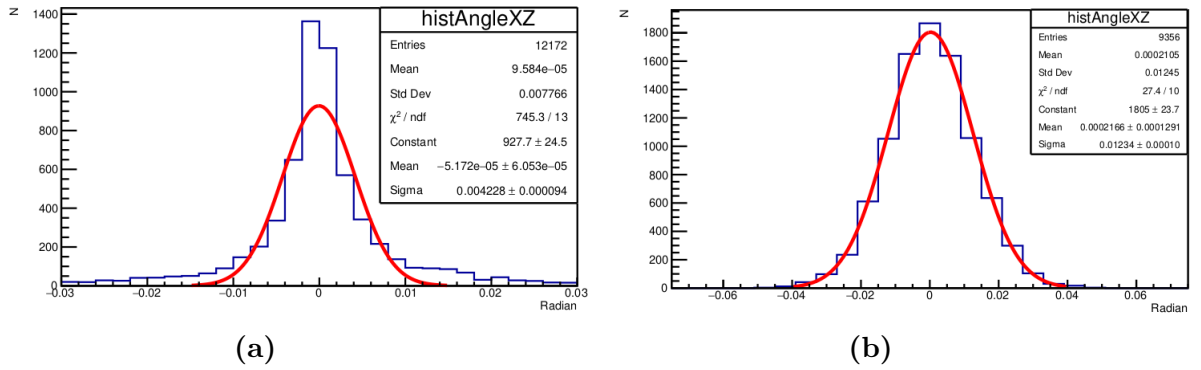


Fig. 2.6: (a) Scattering angle distribution without any target. The standard deviation is 4.2 mrad; (b) The scattering angle distribution for the lead block of $100 \times 100 \times 100 \text{ mm}^3$ size. The obtained standard deviation is 12.34 mrad, which is close to the theoretically calculated value [Table A.2].

Hence, by leveraging the scattering angle distribution, the differentiation of high Z materials becomes feasible, considering that (1.1) is proportional to Z^2 . It's important to note that this method demands prior knowledge of the target material's thickness, making it less practical in real-world scenarios. Nevertheless, its utility can be enhanced by incorporating Points of Closest Approach (POCA) information through voxelization.

Chapter 3

Experimental Studies

3.1 Building the RPC and signal read-out panel

A 2 mm gap Resistive Plate Chamber (RPC) is developed using 200 x 200 x 3 mm^3 size graphite-coated glass plates. A printed circuit board (PCB) based strip read-out panel is developed to read the RPC signals. The procedures are detailed below.

3.1.1 Procedure used to build the RPC

- Two glass plates with dimensions 200 x 200 x 3 mm^3 were thoroughly washed with lab clean soap and distilled water. Then, they are wiped with 2-propanol.
- These glass plates are coated with graphite paint using an INGCO 450 W paint spray gun. The developed electrodes are shown in Figure 3.1a. The surface resistance of the electrodes is measured using a locally made copper zig. The measured surface resistance values across the electrodes are about 1 $M\Omega/\square$. Please see Figure 3.1b.
- The electrodes are separated by placing a 2 mm thick and 10 mm diameter acrylic spacer at the center and 200 mm \times 10 mm \times 2 mm spacers at the edges. Two gas nozzles are placed at the opposite corners of the RPC. Araldite standard epoxy adhesive is applied to the glass and spacers to isolate the RPC gap from the outer atmosphere. This assembly is left for a week for curing. The assembled RPC is shown in Figure 3.2a.

3.1.2 Procedure used to develop RPC signal read-out panel

A 300 mm \times 300 mm \times 1.5 mm copper clad PCB is etched with ferric chloride to develop copper strips. The copper strips are 9 mm in width and 230 mm in length.

- A design was printed with black ink on an A4 sheet. This sheet is placed on the PCB, and then the design is ironed on the PCB. The ink is diffused on the PCB.
- This PCB is placed inside the ferric chloride solution. The copper where ink is not deposited is etched out by the solution. The developed copper strip read-out panel is shown in Figure 3.2b.

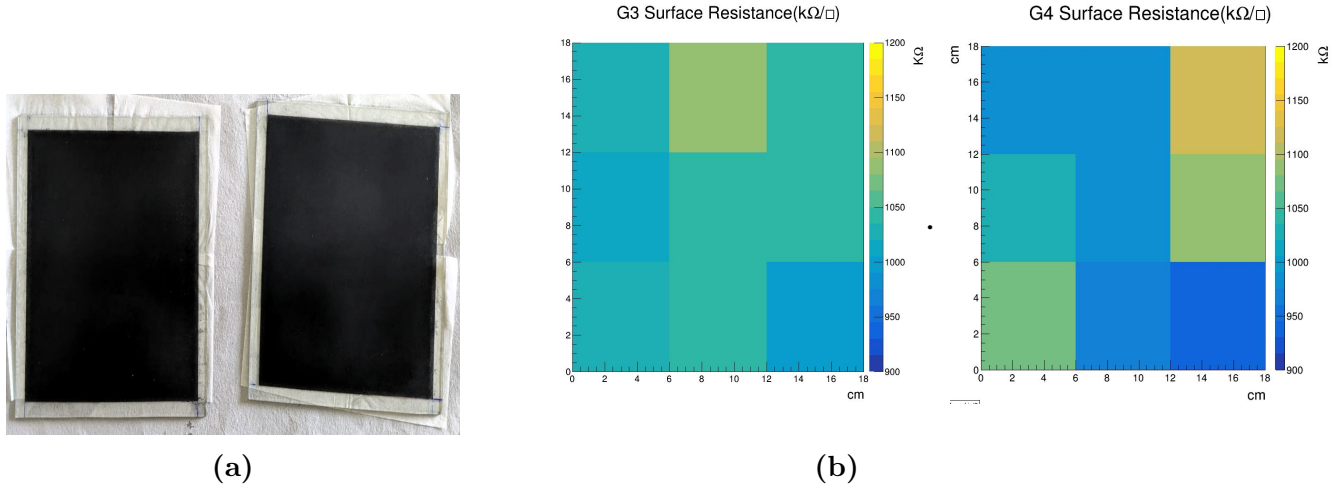


Fig. 3.1: (a) Two graphite-painted glass electrodes. (b) Surface resistance map.

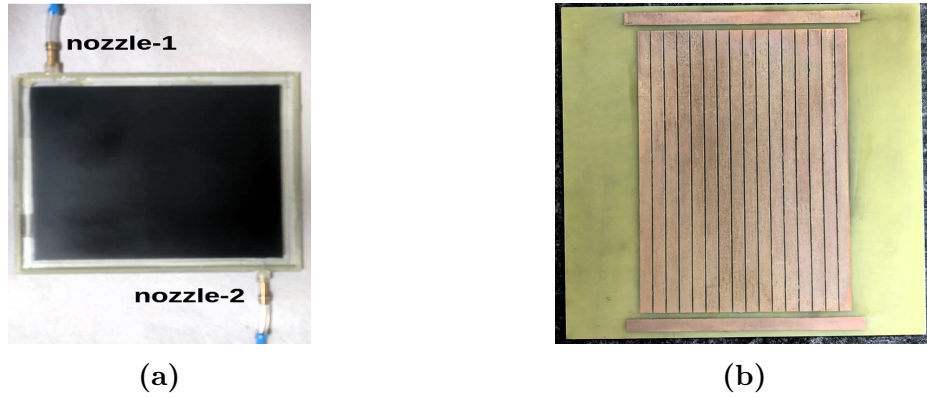


Fig. 3.2: (a) A 2 mm single gap $200 \times 200 \text{ mm}^2$ RPC. The two nozzles will be used as a gas inlet and outlet for RPC and (b) A PCB-based copper strip read-out panel.

3.2 Future Directions

3.2.1 Simulations studies

Apply the voxelization technique for imaging mixtures of different materials, such as lead and uranium. This method helps overcome the limitations of the previous technique, which can not differentiate the material if it is made of two different dense objects and requires the thickness of the target, making it impractical. Voxelization-based imaging can overcome both limitations. In addition, implement the cluster size to the hit position and obtain images and scattering angle distributions for different materials.

3.2.2 Experimental Studies

- Study the RPC's efficiency, charge deposition, and time resolution.
- Read the RPC signals using an ASIC and FPGA-based data acquisition system.

Appendix A

A.1 Time dilation for Cosmic-Ray muons

Pions (π^+ , π^0 , π^-) and Kaons (K^+ , K_S^0 , K_L^0 , K^-) are the subnuclear particles most abundantly produced by these cosmic rays collision with air molecules in upper atmosphere, and when they are charged their dominant decay modes prodEarth'sns : Charged Pions (π^\pm) predominantly decay into muons (μ^\pm) and muon neutrinos (ν_μ or $\bar{\nu}_\mu$) approximately 99.99% of the time. Similarly, charged kaons (K^\pm) decay into muons and muon neutrinos about 64% of the time, with an additional 3% of cases involving the production of a π^0 particle. When charged kaons do not directly decay into muons, they mostly decay into two or three pions ($\pi^\pm\pi^0$, $\pi^\pm\pi^\pm\pi^\mp$, or $\pi^\pm\pi^0\pi^0$), and these pions, if charged, can further decay into muons.

The short-lived K_S^0 particle almost always decays into pion pairs ($\pi^+\pi^-$ or $\pi^0\pi^0$). On the other hand, the long-lived K_L^0 particle can decay into Earthtriplets ($\pi^+\pi^-\pi^0$ or $\pi^0\pi^0\pi^0$). Additionally, K_L^0 produces muons in approximately 27% of its decays through the channel $K_L^0 \rightarrow \pi^\pm\mu^\mp\bar{\nu}_\mu$ (ν_μ).

These decay processes contribute significantly to the production of muons and other particles in the interactions of cosmic rays with the atmosphere, leading to a diverse range of muon flux observations at the Earth's surface. Muon half-life is $2.2\mu\text{s}$ and the average distance between the upper atmosphere and the earth's surface. Hence, one can ask how muons reach in such a short time. When muons are created in the upper atmosphere from interactions of high-energy cosmic rays with atmospheric nuclei, they are typically produced with high velocities close to the speed of light (c). As they move at such relativistic speeds, they experience time dilation, a fundamental concept in Einstein's theory of special relativity. Time dilation means that time appears to pass more slowly for an object in motion relative to an observer at rest.

Due to time dilation, muons moving at relativistic speeds experience time at a slower rate than an observer at rest on Earth. This means that from the perspective of the muon, its lifetime appears to be longer. As a result, muons can travel much farther than they would if they were at rest before decaying. Relativistic Effects on Muons:

The muons have a half-life of 2.2 microseconds. At the speed of light, this would give a range of only 660 m. However, at relativistic speeds, the lifetime of the muon, as we perceive it, is much longer [14]. Given a minimal 2GeV muon (rest mass = 0.1GeV): Kinetic Energy :

$$K = amc^2 - mc^2$$

where $a = \frac{1}{\sqrt{1-\frac{u^2}{c^2}}}$ and u = relative velocity
rearrange :

$$\alpha = \frac{K + mc^2}{mc^2} = \frac{(2 + 0.1)\text{GeV}_{eV}}{0.1\text{GeV}} = 21$$

Using time dilation :

$$\Delta t = a\Delta t'$$

$$\Delta t = 21 \times 2.2 \times 10^{-6} s = 4.6 \times 10^{-5} s$$

Range $x = ct$

$$x = (3.0 \times 10^8 \text{ m/s}) \times (4.6 \times 10^{-5} s) = 13860 \text{ m}$$

Without relativistic effects, muons won't be able to reach Earth's surface. It can travel 660 meters if we don't consider time dilation. However, considering time dilation, it travels ≈ 14 km, the height of generation of CR muons from the sea level.

B.2 Point of Closet Approach

- 1. The shortest line segment between two lines "a" and "b" can be found by minimizing the distance function $\|Pb - Pa\|^2$ and solving the resulting equations for μ_a and μ_b , then substituting these values into the line equations to obtain the intersection points.
- 2. The shortest line segment between two lines is perpendicular to both lines. This line segment can be determined by finding the direction vector of each line and taking their cross-product to get the direction vector of the shortest line. The point of intersection of this shortest line with one of the given lines can then be calculated, and it will give the coordinates of the nearest point on that line.

The dot product equations for finding the shortest line segment between two lines are:

$$(Pa - Pb) \cdot (P2 - P1) = 0$$

$$(Pa - Pb) \cdot (P4 - P3) = 0$$

Expanding these equations with the line equations:

$$(P1 - P3 + \mu_a(P2 - P1) - \mu_b(P4 - P3)) \cdot (P2 - P1) = 0$$

$$(P1 - P3 + \mu_a(P2 - P1) - \mu_b(P4 - P3)) \cdot (P4 - P3) = 0$$

$$(P1 - P3) \cdot (P2 - P1) + \mu_a(P2 - P1) \cdot (P2 - P1) - \mu_b(P4 - P3) \cdot (P2 - P1) = 0$$

$$(P1 - P3) \cdot (P4 - P3) + \mu_a(P2 - P1) \cdot (P4 - P3) - \mu_b(P4 - P3) \cdot (P4 - P3) = 0$$

The equations for finding μ_a and μ_b , which determine the shortest line segment between two lines, are:

$$\mu_a = (d_{1343} d_{4321} - d_{1321} d_{4343}) / (d_{2121} d_{4343} - d_{4321} d_{4321})$$

$$\mu_b = (d_{1343} + \mu_a * d_{4321}) / d_{4343}$$

where $d_{mnop} = (x_m - x_n)(x_o - x_p) + (y_m - y_n)(y_o - y_p) + (z_m - z_n)(z_o - z_p)$.

C.3 Simulation Setup

- For building geometry, we used G4VUserDetectorConstruction abstract base class and derived our class, "DetectorConstruction".
- In this class, "DetectorConstruction" a Construct() method was implemented.

- Construct all necessary materials using G4Material. Some materials are already available in the NIST manager[15], and if it is not, we can build them by ourselves for example, CO2: // creating CO2

```
G4double a = 12 * g / mole; // carbon
```

```
G4int z;
```

```
G4Element *elC = new G4Element("Carbon", "C", z = 6, a);
```

```
a = 16.00 * g / mole; //
```

```
G4Element *elO = new G4Element("Oxygen", "O", z = 8, a);
```

```
G4double density;
```

```
G4int n;
```

```
G4Material *CO2 = new G4Material("Carbon Dioxide", density = 1.87 * g / cm3, n = 2);
```

```
G4int nAtoms; CO2->AddElement(elC, nAtoms = 1);
```

```
CO2->AddElement(elO, nAtoms = 2);
```

- In this way, we can define several mixtures of gases and test them.
- we have used two mixtures: 1. Argon(70%)+CO2(30%) and 2. R134A (95.2%)+Butane(4.5%)+SF6(0.3%)
- Define shapes/solids
- Define logical volumes
- Place volumes of your detector geometry
- Instantiate sensitive detectors/scorers and set them to corresponding volumes (optional)
- Define visualization attributes for the detector elements (optional)
- Define regions (optional)

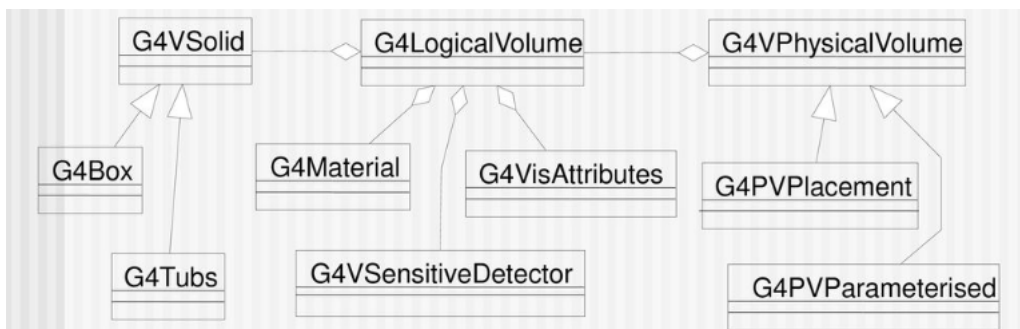


Fig. A.1: Basic Structure for defining geometry

D.4 Differentiating high-Z material (Iron, Lead and Uranium, Iron) using Muon Scattering Tomography (MST)

Table A.1: Properties of selected elements

Element	Atomic Mass (u)	Atomic Number(Z)	Density (g/cm ³)	Radiation Length [16] (cm)
Iron	55.8	26	7.87	1.76
Lead	207.2	82	11.34	0.56
Uranium	238.0	92	19.05	0.31

Table A.2: Comparison of theoretically (1.1) calculated and simulated sigma values for different materials of thickness 10 cm.

Material (Z)	$\sigma_{\text{theoretical}}(\text{mrad})$	$\sigma_{\text{simulation}}(\text{mrad})$
Iron (26)	6.65	6.62
Lead (82)	12.05	12.34
Uranium (92)	16.82	16.60

With the increase of the atomic number of target material, the standard deviation in the scattering angle distributions increased.

D.4.1 Scattering angle distribution for an iron block of size $100 \times 100 \times 100 \text{ mm}^3$

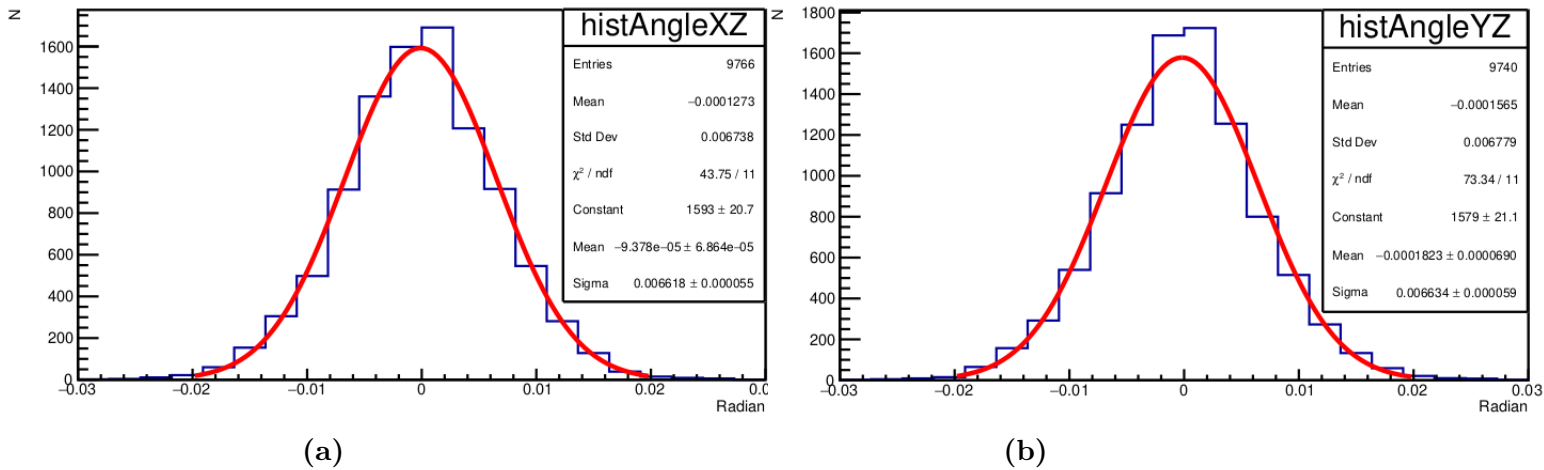


Fig. A.2: (a) Scattering angle distribution in XZ plane. (b) Scattering angle distribution in YZ plane.

D.4.2 Scattering angle distribution for uranium block size $100 \times 100 \times 100 \text{ mm}^3$

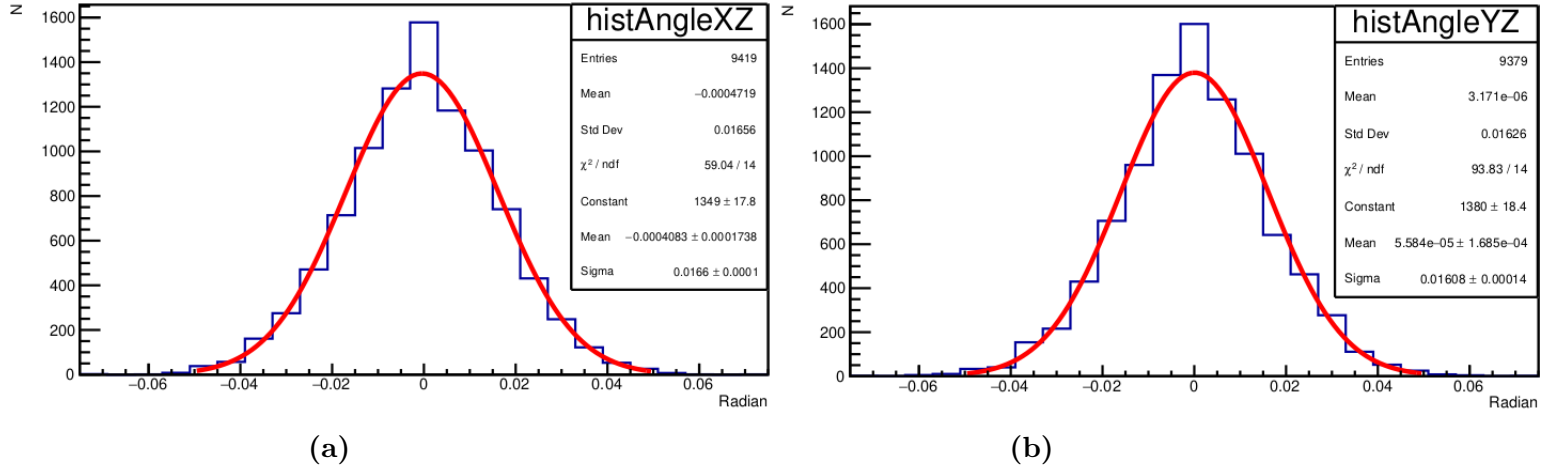


Fig. A.3: (a) Scattering angle distribution in XZ plane. (b) Scattering angle distribution in YZ plane.

Bibliography

- [1] G. Bonomi, P. Checchia, M. D’Errico, D. Pagano, and G. Saracino. Applications of cosmic-ray muons. *Progress in Particle and Nuclear Physics*, 112:103768, 2020.
- [2] Lorenzo Bonechi, Raffaello D’Alessandro, and Andrea Giammanco. Atmospheric muons as an imaging tool. *Reviews in Physics*, 5:100038, 2020.
- [3] E. Rutherford. Lxxix. the scattering of α and β particles by matter and the structure of the atom. *The London, Edinburgh, and Dublin Philosophical Magazine and Journal of Science*, 21(125):669–688, 1911.
- [4] K. Raveendrababu. *Study of glass resistive plate chambers for the INO-ICAL detector*. PhD thesis, Tata Institute of Fundamental Research, 2016. Accessed: 14th November 2023.
- [5] R. Santonico and R. Cardarelli. Development of resistive plate counters. *Nuclear Instruments and Methods in Physics Research*, 187(2):377–380, 1981.
- [6] The ATLAS Collaboration. The atlas experiment at the cern large hadron collider. *Journal of Instrumentation*, 3(08):S08003, aug 2008.
- [7] R. Adolphi et al. The CMS experiment at the CERN LHC. *JINST*, 3:S08004, 2008.
- [8] S. Agostinelli, J. Allison, K. Amako, J. Apostolakis, H. Araujo, P. Arce, M. Asai, D. Axen, S. Banerjee, G. Barrand, F. Behner, L. Bellagamba, J. Boudreau, L. Broglia, A. Brunengo, H. Burkhardt, S. Chauvie, J. Chuma, R. Chytrcek, G. Cooperman, G. Cosmo, P. Degt-yarenko, A. Dell’Acqua, G. Depaola, D. Dietrich, R. Enami, A. Feliciello, C. Ferguson, H. Fesefeldt, G. Folger, F. Foppiano, A. Forti, S. Garelli, S. Giani, R. Giannitrapani, D. Gibin, J.J. Gómez Cadenas, I. González, G. Gracia Abril, G. Greeniaus, W. Greiner, V. Grichine, A. Grossheim, S. Guatelli, P. Gumplinger, R. Hamatsu, K. Hashimoto, H. Ha-sui, A. Heikkinen, A. Howard, V. Ivanchenko, A. Johnson, F.W. Jones, J. Kallenbach, N. Kanaya, M. Kawabata, Y. Kawabata, M. Kawaguti, S. Kelner, P. Kent, A. Kimura, T. Kodama, R. Kokoulin, M. Kossov, H. Kurashige, E. Lamanna, T. Lampén, V. Lara, V. Lefebure, F. Lei, M. Liendl, W. Lockman, F. Longo, S. Magni, M. Maire, E. Medernach, K. Minamimoto, P. Mora de Freitas, Y. Morita, K. Murakami, M. Nagamatu, R. Nartallo, P. Nieminen, T. Nishimura, K. Ohtsubo, M. Okamura, S. O’Neale, Y. Oohata, K. Paech, J. Perl, A. Pfeiffer, M.G. Pia, F. Ranjard, A. Rybin, S. Sadilov, E. Di Salvo, G. Santin, T. Sasaki, N. Savvas, Y. Sawada, S. Scherer, S. Sei, V. Sirotenko, D. Smith, N. Starkov, H. Stoecker, J. Sulkimo, M. Takahata, S. Tanaka, E. Tcherniaev, E. Safai Tehrani, M. Tro-peano, P. Truscott, H. Uno, L. Urban, P. Urban, M. Verderi, A. Walkden, W. Wander, H. Weber, J.P. Wellisch, T. Wenaus, D.C. Williams, D. Wright, T. Yamada, H. Yoshida, and D. Zschesche. Geant4—a simulation toolkit. *Nuclear Instruments and Methods in Physics Research Section A: Accelerators, Spectrometers, Detectors and Associated Equip-ment*, 506(3):250–303, 2003.

- [9] Rene Brun, Fons Rademakers, Philippe Canal, Axel Naumann, Olivier Couet, Lorenzo Moneta, Vassil Vassilev, Sergey Linev, Danilo Piparo, Gerardo GANIS, Bertrand Belenot, Enrico Guiraud, Guilherme Amadio, wverkerke, Pere Mato, TimurP, Matevž Tadel, wlav, Enric Tejedor, Jakob Blomer, Andrei Gheata, Stephan Hageboeck, Stefan Roiser, marsupial, Stefan Wunsch, Oksana Shadura, Anirudha Bose, CristinaCristescu, Xavier Valls, and Raphael Isemann. root-project/root: v6.18/02, June 2020.
- [10] Abhishek NISER . Muoscope.Project.2023. https://github.com/abhich2507/Muoscope_Project_2023, 2023. Accessed: December 16, 2023.
- [11] D Pagano, G Bonomi, A Donzella, A Zenoni, G Zumerle, and N Zurlo. EcoMug: An efficient COsmic MUon generator for cosmic-ray muon applications. *Nucl. Instrum. Methods Phys. Res. A*, 1014(165732):165732, October 2021.
- [12] CMS Collaboration. Measurement of the charge ratio of atmospheric muons with the cms detector. *Physics Letters B*, 692(2):83–104, 2010.
- [13] Paul Bourke. Geometry in computer graphics - point, line, plane, October 1988. Accessed: November 14th, 2023.
- [14] M. P. Balandin, V. M. Grebenyuk, V. G. Zinov, A. D. Konin, and A. N. Ponomarev. Measurement of the lifetime of the positive muon. *Soviet Journal of Experimental and Theoretical Physics*, 40:811, November 1975.
- [15] National Institute of Standards and Technology. Security requirements for cryptographic modules. Technical Report Federal Information Processing Standards Publications (FIPS PUBS) 140-2, Change Notice 2 December 03, 2002, U.S. Department of Commerce, Washington, D.C., 2001.
- [16] Particle Data Group. Particle data group, 2012. Accessed: November 14th, 2023.
- [17] L.J. Schultz, K.N. Borozdin, J.J. Gomez, G.E. Hogan, J.A. McGill, C.L. Morris, W.C. Priedhorsky, A. Saunders, and M.E. Teasdale. Image reconstruction and material z discrimination via cosmic ray muon radiography. *Nuclear Instruments and Methods in Physics Research Section A: Accelerators, Spectrometers, Detectors and Associated Equipment*, 519(3):687–694, 2004.
- [18] L Bonechi. *Misure di raggi cosmici a terra con l’esperimento ADAMO*. PhD thesis, University of Florence Florence, Italy, 2004.
- [19] Ken Mimasu and Verónica Sanz. Alps at colliders, 2014.